SCIENTIFIC REP🌼RTS

OPEN

First Introduction of NiSe$_2$ to Anode Material for Sodium-Ion Batteries: A Hybrid of Graphene-Wrapped NiSe$_2$/C Porous Nanofiber

Jung Sang Cho, Seung Yeon Lee & Yun Chan Kang

The first-ever study of nickel selenide materials as efficient anode materials for Na-ion rechargeable batteries is conducted using the electrospinning process. NiSe$_2$-reduced graphene oxide (rGO)-C composite nanofibers are successfully prepared via electrospinning and a subsequent selenization process. The electrospun nanofibers giving rise to these porous-structured composite nanofibers with optimum amount of amorphous C are obtained from the polystyrene to polyacrylonitrile ratio of 1/4. These composite nanofibers also consist of uniformly distributed single-crystalline NiSe$_2$ nanocrystals that have a mean size of 27 nm. In contrast, the densely structured bare NiSe$_2$ nanofibers formed via selenization of the pure NiO nanofibers consist of large crystallites. The initial discharge capacities of the NiSe$_2$-rGO-C composite and bare NiSe$_2$ nanofibers at a current density of 200 mA g^{-1} are 717 and 755 mA h g^{-1}, respectively. However, the respective 100th-cycle discharge capacities of the former and latter are 468 and 35 mA h g^{-1}. Electrochemical impedance spectroscopy measurements reveal the structural stability of the composite nanofibers during repeated Na-ion insertion and extraction processes. The excellent Na-ion storage properties of these nanofibers are attributed to this structural stability.

Next-generation rechargeable batteries have been extensively studied as a potential power source for large-scale devices such as electric vehicles (EVs), hybrid electric vehicles (HEVs), and smart grids[1–4]. In addition, Na-ion batteries (NIBs) have recently received significant attention owing to their low cost and abundant global reserves compared to those of Li-ion batteries (LIBs)[5–10]. However, Na ion have a larger ionic radius and molar mass than Li ion; hence, NIBs exhibit lower specific capacity and rate capability, larger volume change, and shorter cycling life than LIBs[11–13]. Moreover, carbonaceous materials are typically used as anode materials for commercial LIBs, but their low reversible capacity and Na plating behavior render them unsuitable for NIBs[14,15]. The development of efficient anode materials with high reversible capacity as well as excellent cycle and high rate performance is therefore essential for the commercialization of NIBs.

Recently, metal chalcogenide materials including metal sulfides and selenides have been successfully applied as anode materials for NIBs[16–19]. Nanostructured metal sulfides with various compositions and their carbon composite materials have, in fact, been used in many synthesis processes, including the hydrothermal[8,20,21], solvothermal[22], mechanical alloying[23], chemical vapor deposition[24], liquid-phase exfoliation methods[25], and spray pyrolysis[26]. However, the synthesis of nanostructured metal selenides and their carbon composite materials for use in NIBs has been scarcely studied. In one of the few studies conducted, Ko *et al.* used a spray pyrolysis process to fabricate yolk-shell-structured MoSe$_2$ microspheres as an anode material for NIBs; these microspheres delivered a 50th-cycle discharge capacity of 433 mA h g^{-1} at a current density of 0.2 A g^{-1}[27]. Zhang *et al.* used a simple hydrothermal method to fabricate nanooctahedra-assembled FeSe$_2$ microspheres that delivered a stable discharge capacity of 372 mA h g^{-1} after 2000 cycles at 1 A g^{-1}[17]. Furthermore, a SnSe-carbon composite formed through a facile ball milling process exhibited a high reversible capacity of 707 mA h g^{-1} at a current density of 143 mA g^{-1} (~0.2 C) and stable cycle performance over 50 cycles[19]. Carbon- and non-carbon-containing nickel sulphide materials have also been extensively studied as anode materials for NIBs[28]. However, to the best of our knowledge, nickel selenide (NiSe$_2$) materials have not been investigated as anode materials for NIBs.

Department of Materials Science and Engineering, Korea University, Anam-Dong, Seongbuk-Gu, Seoul 136-713, Republic of Korea. Correspondence and requests for materials should be addressed to Y.C.K. (email: yckang@korea.ac.kr)
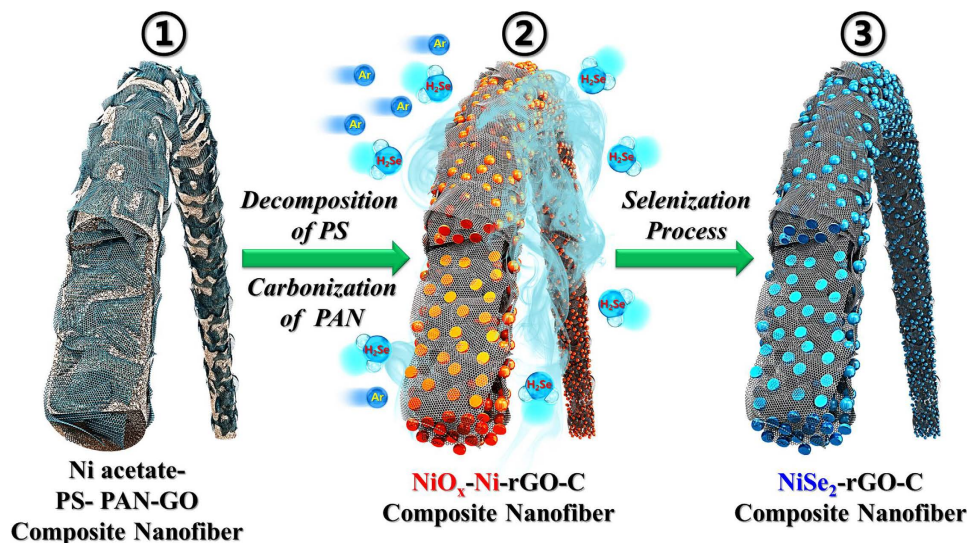
Figure 1. Formation mechanism of the NiSe$_2$ nanoparticle-decorated rGO-C composite nanofibers.

Electrospinning is a simple and highly versatile method used for the preparation of one-dimensional nanostructures of various compositions[29–32]. Therefore, various carbon- and non-carbon-containing transition metal sulfide materials have been prepared via the electrospinning process as anode materials for LIBs and NIBs[33–35]. Metal selenide materials designated for use in rechargeable batteries have, however, not been prepared via the electrospinning process. As such, in this study, NiSe$_2$-reduced graphene oxide (rGO)-carbon composite porous nanofibers were prepared via an electrospinning and subsequent selenization process. Porous nanostructure could enhance the contact area between the host materials (NiSe$_2$) and the electrolyte, additionally shorten the diffusion paths of the electrons and Na$^+$ during cycling[36,37]. Moreover, porous structure accommodates the volume change of NiSe$_2$ to alleviate pulverization during cycling[36,37]. Along with this, graphene has been considered as the most promising carbon matrix to support anode materials in LIBs due to its superior electrical conductivity and high mechanical strength[38]. Amorphous carbon was also incorporated into NiSe$_2$-reduced graphene oxide system to effectively alleviate the aggregation of NiSe$_2$ nanoparticles by separating them from each other and helped reduced graphene oxide build more-efficient 3D conducting networks. The composite nanofibers composed of Ni salt, GO nanosheets, polystyrene (PS), and polyacrylonitrile (PAN) were transformed into the NiSe$_2$-rGO-C composite nanofibers by using a simple selenization process.

Results and Discussion

The formation mechanism of the NiSe$_2$ nanoparticle-decorated rGO-C composite nanofibers is illustrated in Fig. 1. Under the Ar atmosphere, low conductive amorphous C is produced by the carbonization of PAN and the PS is decomposed into gases. Electrospun nanofibers formed from the solution containing only PAN as an organic polymer, result therefore in C composite nanofibers with high C content. On the other hand, the PS melted before being decomposed into gases during the post-treatment of electrospun nanofibers formed from the solution containing only PS as an organic polymer; this resulted in the formation of stacked and irregular nanofibers. In this study, an optimum PS to PAN ratio of 1/4 was used to form the stable polymeric nanofibers during the post-treatment process. Highly porous NiO$_x$-Ni-rGO-C composite nanofibers were formed by post-treating the electrospun nanofibers formed from the colloidal DMF solution containing Ni acetate, PS, PAN, and GO nanosheets, at 450 °C under an Ar atmosphere. Subsequent selenization of these composite nanofibers at 300 °C under H$_2$Se gas gives rise to the NiSe$_2$-rGO-C composite nanofibers, in which NiSe$_2$ nanocrystals are uniformly distributed throughout the rGO-C composite nanofibers.

The effect of the PS on the morphologies of the electrospun nanofibers before and after the post-treatment is shown in Figs S1 and S2. As Fig. S1a shows, the electrospun nanofibers formed from the colloidal DMF solution containing Ni acetate, PS, PAN, and GO nanosheets have a uniform morphology. The electrospun nanofibers formed from the DMF solution containing Ni acetate and PAN only also had a uniform morphology (Fig. S2a). Furthermore, owing to the elimination of PS via decomposition, nanofibers having a porous wood pulp, fiber-like structure formed when the electrospun nanofibers containing GO nanosheets were post-treated under an Ar atmosphere; the formation of the porous structure was also affected by the nanosheets. However, the electrospun nanofibers formed from the DMF solution containing Ni acetate and PAN only, had a uniform morphology even after a post-treatment at 450 °C under air atmosphere. The corresponding XRD pattern (Fig. S2c) revealed that phase-pure NiO nanofibers formed after this post-treatment.

Figure 2 shows the morphologies of the NiSe$_2$-rGO-C composite nanofibers resulting from the selenization of the nanofibers shown in Fig. S1. As Fig. 2a,b show, the wood pulp fiber-like porous structure of the nanofibers persists even after the selenization process. The low-resolution TEM images (Fig. 2c,d) revealed that ultrafine NiSe$_2$ nanocrystals are uniformly distributed over the surface of the composite nanofibers. These nanocrystals have a single-crystalline structure (Fig. 2e,f), as revealed by the high-resolution images. They also exhibit
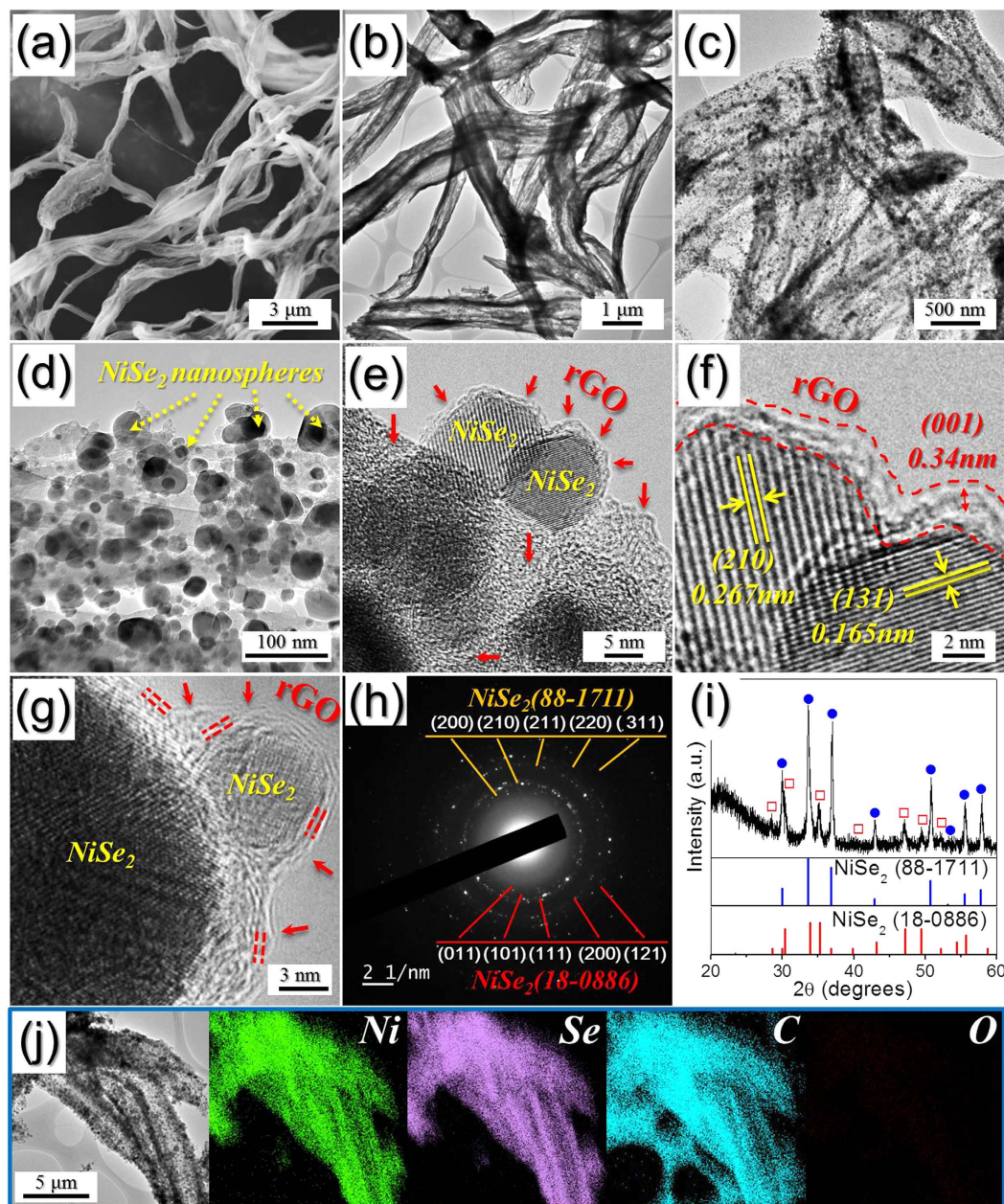
Figure 2. Morphologies, SAED pattern, XRD pattern, and elemental mapping images of the NiSe₂-rGO-C composite nanofibers formed by selenization process of the carbonized nanofibers. (**a**) SEM image, (**b–d**) TEM images, (**e–g**) HR-TEM images, (**h**) SAED pattern, (**i**) XRD pattern, and (**j**) elemental mapping images.

clear 0.267- and 0.165-nm-spaced lattice fringes, which correspond to the (210) and (131) crystal planes of the cubic and orthorhombic $NiSe_2$ phases, respectively; stacked multi-layer rGO was also observed in the images, as indicated by the arrows in Fig. 2e,g. In addition, the SAED and XRD patterns (Fig. 2h,i) indicate that the $NiSe_2$-rGO-C composite nanofibers have mixed crystal structures of cubic and orthorhombic $NiSe_2$ phases. The broad XRD peaks shown in Fig. 2i are attributed to the formation of the ultrafine $NiSe_2$ nanocrystals that have a mean size of 27 nm, as determined from the TEM images. Furthermore, energy dispersive spectroscopy (EDS) analysis revealed that the composite nanofibers (Fig. S3) had a Ni-to-Se component ratio of ~2. The corresponding elemental mapping images (Fig. 2j) show that the $NiSe_2$ nanocrystals are uniformly distributed throughout the rGO-C matrix, as revealed previously by the TEM images. Moreover, D and G bands corresponding to graphene occur at 1340 and 1605 cm^{-1}, respectively, in the Raman spectrum (Fig. S4). The higher signal peak intensity of the D band compared to that of the G band, is indicative of the thermal reduction of GO nanosheets to rGO nanosheets during the two-step post-treatment process. In addition, carbonization of the PAN and consequent formation of amorphous C resulted in an increase in the intensity of the peak corresponding to the D band. The TG curve of the $NiSe_2$-rGO-C composite nanofibers shown in Fig. S5 revealed a three-step weight loss for temperatures below 600 °C. The weight loss observed at temperatures between 350 and 600 °C was attributed

to the decomposition of $NiSe_2$ into NiO and the combustion of rGO and amorphous C. The rGO and amorphous C contents of 25% was estimated from the TG analysis of the $NiSe_2$-rGO-C composite nanofibers. The chemical state and molecular environment of the $NiSe_2$-rGO-C composite nanofibers were characterized via X-ray photoelectron spectroscopy (XPS). The resulting XPS survey spectrum (Fig. S6) exhibited Ni, Se, and C signals. In fact, the main peaks of the Ni 2p spectrum (Fig. S6a) occurred at binding energies of 853.5 eV and 873.4 eV corresponding to Ni $2p_{3/2}$ and Ni $2p_{1/2}$, respectively; these are characteristic of $NiSe_2$ and two shake-up satellites. A peak at a binding energy of 54.5 eV in the Se 3d spectrum (Fig. S6b) also confirmed the presence of $NiSe_2$ in the composite nanofibers, in accordance with previous studies[39]. Furthermore, the C 1s spectrum (Fig. S6c) exhibits peaks corresponding to sp^2-bonded carbon (C–C), epoxy and alkoxy groups (C–O), and carbonyl and carboxylic (C=O) components at 284.6, 286.6, and 288.1 eV, respectively; the peak corresponding to the C–C bond exhibits high intensity, whereas those associated with the C–O and C=O bonds have low intensities. This indicates that the GO nanosheets undergo thermal reduction to rGO nanosheets during the two-step post-treatment preparation process[40,41].

The SEM and TEM images (Fig. 3) show the morphologies of the bare $NiSe_2$ nanofibers formed via selenization of the nanofibers shown in Fig. S2; these densely structured (i.e., non-porous) nanofibers are formed when pure NiO nanofibers are selenized. Moreover, the SAED and XRD patterns (Fig. 3e,f) reveal that the $NiSe_2$ nanofibers are cubic and phase-pure (i.e., do not contain impurity phases). The elemental mapping images also (Fig. 3g) confirm that these $NiSe_2$ nanofibers, formed via the two-step post-treatment process of the Ni acetate-PAN electrospun nanofibers, are C-free. The BET surface areas of the bare $NiSe_2$ and $NiSe_2$-rGO-C composite nanofibers were 21 and 119 $m^2 g^{-1}$, respectively (Fig. S7).
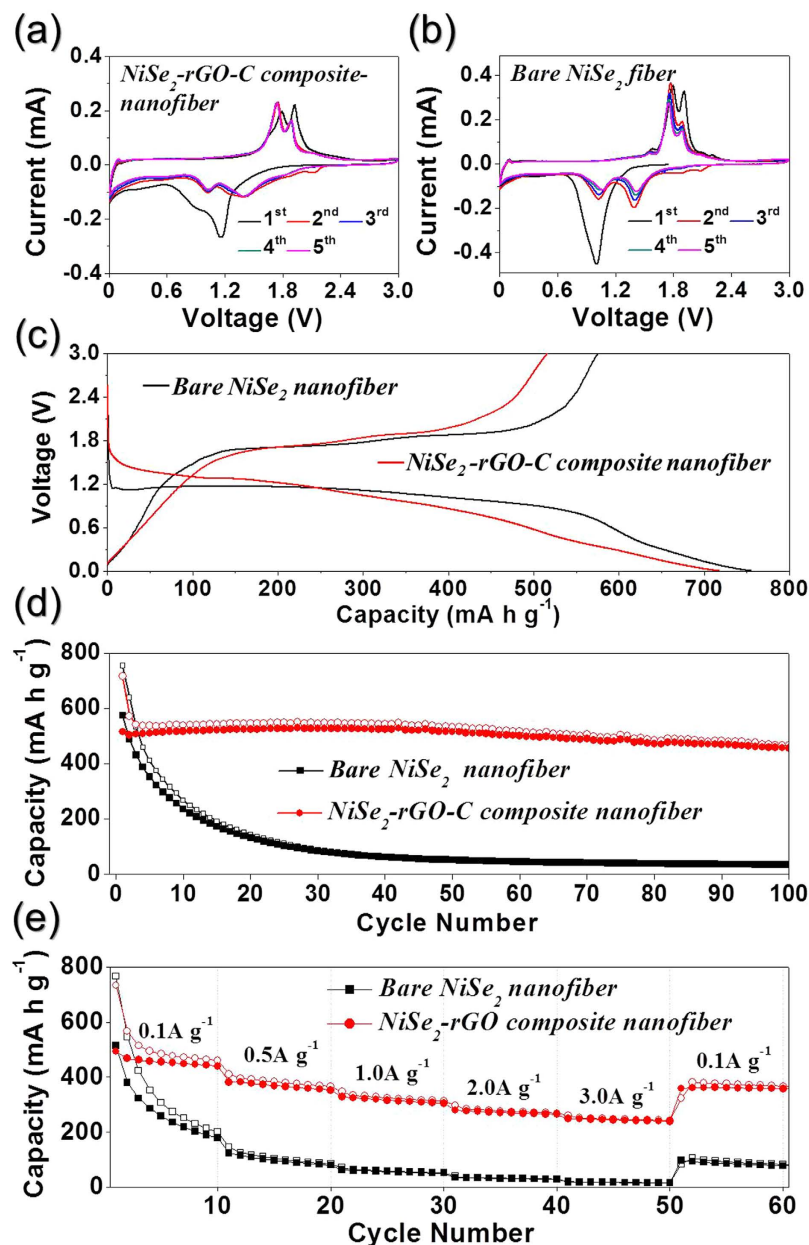
The electrochemical properties of the $NiSe_2$-rGO-C composite nanofibers for Na-ion storage were compared with those of the densely structured $NiSe_2$ nanofibers; this comparison was made via cyclic voltammograms (CVs) and galvanostatic discharge/charge cycling at voltages ranging from 0.001–3 V vs. Na/Na^+. Figure 4a,b show the CV curves obtained at a scan rate of 0.07 mV s^{-1} from the first five cycles of the $NiSe_2$-rGO-C composite and bare $NiSe_2$ nanofibers, respectively. The first cathodic scan of the $NiSe_2$-rGO-C composite nanofibers exhibited two broad peaks at 1.2 and 0.9 V. However, the Na-ion insertion and desertion mechanisms of $NiSe_2$ have not been identified in previous studies and therefore, the electrochemical reaction of $NiSe_2$ for Na-ion storage was estimated from that of NiS[28]. The reaction of NiS with Na proceeds as follows: $NiS + 2Na \leftrightarrow Na_2S + Ni$[28]. The reduction peaks located at 1.2 and 0.9 V may therefore be attributed to the formation of $NiSe_x$ and Na_2Se, and Ni and Na_2Se, respectively. During the anodic scans, two oxidation peaks, which may be attributed to the formation of $NiSe_x$ and $NiSe_2$, occurred at respective voltages of 1.8 and 1.9 V. A broad reduction peak (Fig. 4b) occurs at a potential of ~ 1.0 V during the first cathodic scan of the bare $NiSe_2$ nanofibers. However, the reduction peaks of both the bare and composite nanofibers shifted to higher voltages than those associated with the first cycle; these shifts resulted from the improved kinetics of the electrode owing to the formation of ultrafine nanoclusters after the first cycle. The significant overlapping of the CV curves from the second cycle onward (Fig. 4a) indicated the excellent cycling stability of the $NiSe_2$-rGO-C composite nanofibers. In contrast, the intensities of the peaks in the reduction and oxidation curves (Fig. 4b) of the bare $NiSe_2$ nanofibers decreased during the first five cycles. The initial discharge and charge curves obtained at a current density of 200 mA g^{-1} are compared in Fig. 4c. The discharge curve of the bare $NiSe_2$ nanofibers exhibits a clear plateau at ~ 1.2 V, whereas that of the $NiSe_2$-rGO-C composite nanofibers decreases monotonically without clear plateaus. The different crystallite sizes of the two samples changed the shapes of the initial discharge curves. The bare and composite nanofibers consist of coarse and fine crystallites, respectively. They also exhibit respective initial discharge capacities of 717 and 755 mA h g^{-1}, and charge capacities of 516 and 575 mA h g^{-1}. The rGO and amorphous C with low Na-ion storage capability led to a reduction in the initial discharge capacity and Coulombic efficiency of the composite nanofibers. Fig. 4d shows the cycling performance of the nanofibers at a current density of 200 mA g^{-1}; the discharge capacities of the $NiSe_2$-rGO-C nanofibers remained at high levels for 100 cycles, whereas those of their bare $NiSe_2$ counterparts decreased sharply to 90 mA h g^{-1} during the first 30 cycles. In fact, the former and latter had 100th-cycle discharge capacities of 468 and only 35 mA h g^{-1}, respectively. The rate performances of the both samples are shown in Fig. 4e, in which the current density is increased step-wise from 0.1 to 3.0 A g^{-1}. The $NiSe_2$-rGO-C composite nanofibers had superior rate capability compared to that of the bare $NiSe_2$ nanofibers. As the figure shows, the composite nanofibers had final discharge capacities of 461, 365, 313, 269, and 243 mA h g^{-1} at current densities of 0.1, 0.5, 1.0, 2.0, and 3.0 A g^{-1}, respectively. These capacities were almost recovered to 383 mA h g^{-1} when the current density was returned to 0.1 A g^{-1} after cycling at high current densities.

The basis for the superior Na-ion storage properties of the composite nanofibers compared to those of their bare counterparts was determined by performing EIS measurements before and after cycling of the nanofibers. These measurements were performed at room temperature before and after 1, 20, and 50 cycles at a current density of 200 mA g^{-1}. The resulting Nyquist plots (Fig. 5) are characterized by semi-circles in the medium-frequency range, which are attributed to the charge-transfer resistance (R_{ct}) of the electrodes[42,43]. The precise values of R_{ct} are calculated from a simulated equivalent circuit. Prior to cycling, the porous highly conductive $NiSe_2$-rGO-C composite nanofibers had a lower R_{ct} of 373 Ω (Fig. 5a) than 587 Ω of the bare $NiSe_2$ nanofibers. The synergetic effect of the porous nanostructure and a graphitic carbon resulted in the low R_{ct} of the $NiSe_2$-rGO-C composite nanofibers. The R_{ct} of $NiSe_2$-rGO-C composite and bare $NiSe_2$ nanofibers decreased to 53 and 81 Ω after the first cycle, respectively, owing to transformation of the $NiSe_2$ crystals into ultrafine nanocrystals during first cycling[44]. In contrast, the R_{ct} of the bare $NiSe_2$ nanofibers increased significantly from 155 to 210 Ω as the number of cycles increases from 20th to 50th cycle, as shown in Fig. 5b. However, the R_{ct} of the $NiSe_2$-rGO-C composite nanofibers remained approximately constant (Fig. 5c) for 50 cycles. These results are indicative of the structural stability of the $NiSe_2$-rGO-C composite nanofibers during repeated Na^+ insertion and extraction processes. In contrast, the loss of structural stability during cycling increased the R_{ct} values of the bare $NiSe_2$ nanofibers.
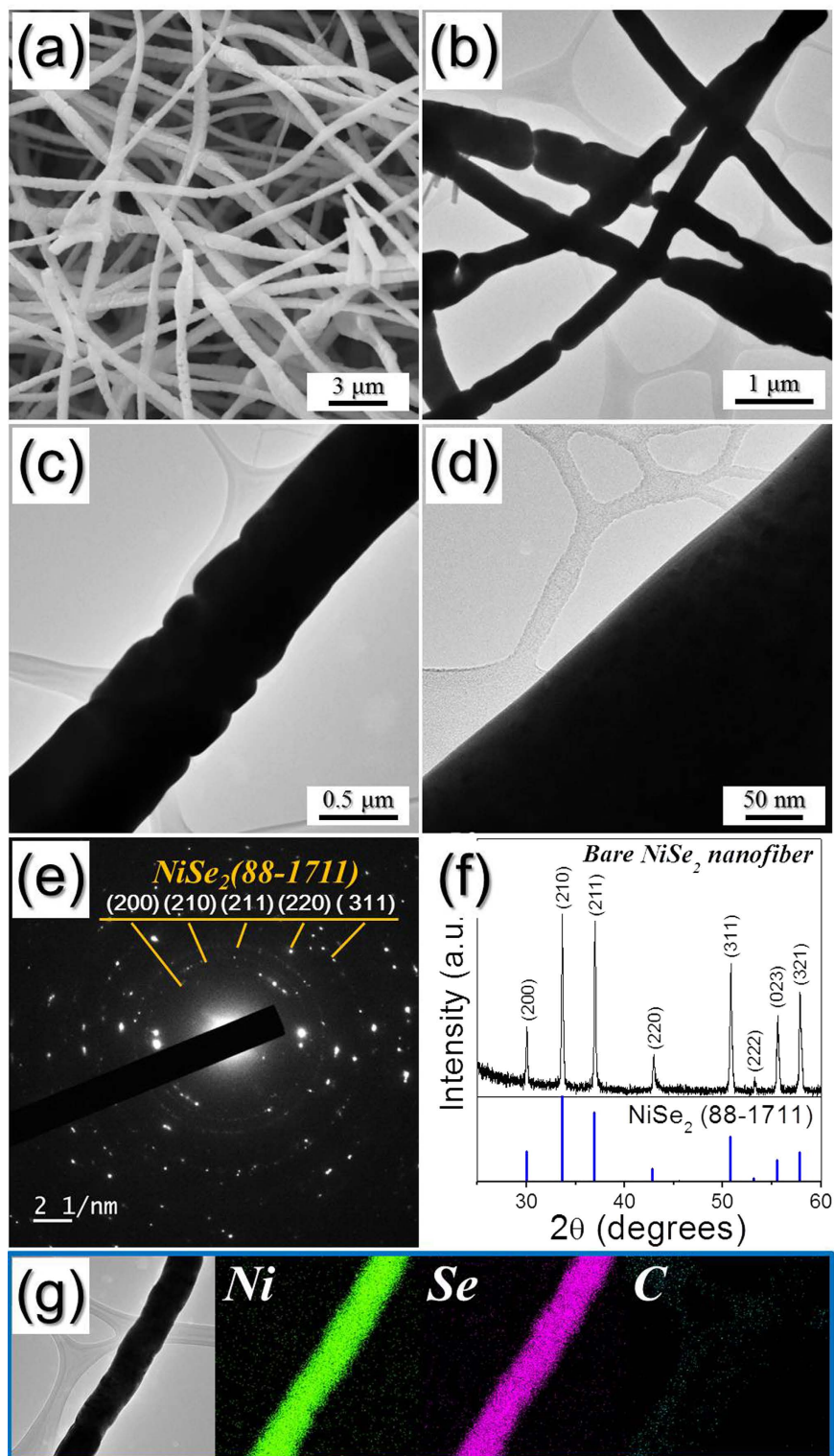
Figure 3. Morphologies, SAED pattern, XRD pattern, and elemental mapping images of the bare NiSe$_2$ nanofibers formed by selenization process of the nanofibers. (**a**) SEM image, (**b–d**) TEM images, (**e**) SAED pattern, (**f**) XRD pattern, and (**g**) elemental mapping images.

To support this proof obviously, the morphologies of the NiSe$_2$-rGO-C composite nanofibers and densely structured NiSe$_2$ nanofibers obtained after 100 cycles are shown in Fig. 6. The NiSe$_2$-rGO-C composite nanofibers maintained their original morphologies even after repeated sodium ion insertion and desertion processes as shown by Fig. 6a. In contrast, the structure of the bare NiSe$_2$ nanofibers with dense structure was broken into

**Figure 4. Electrochemical properties of the NiSe$_2$-rGO-C composite nanofibers and dense structured bare NiSe$_2$ nanofibers for sodium ion storage.** (**a**) cyclic voltammogram (CV) curves of NiSe$_2$-rGO-C composite nanofibers, (**b**) CV curves of bare NiSe$_2$ nanofibers, (**c**) initial charge/discharge curves at a constant current density of 200 mA g^{-1}, (**d**) cycling performances at a constant current density of 200 mA g^{-1}, and (**e**) rate performances.

several pieces after cycling in Fig. 6b. The destruction of the solid NiSe$_2$ nanofibers during cycling decreased the electrical contact with the copper foil electrode. The excellent Na-ion storage properties of the NiSe$_2$-rGO-C composite nanofibers are therefore attributed to this structural stability.

Conclusions

The first-ever investigation of NiSe$_2$ materials for use in Na-ion batteries was conducted in this work. Porous-structured NiSe$_2$-rGO-C composite nanofibers with appropriate amounts of amorphous C were prepared by optimizing the composition of the organic polymers used in the electrospinning process. The high density of polystyrene, which could be decomposed into gases even under an Ar atmosphere, enabled the formation of porous-structured NiSe$_2$-rGO-C composite nanofibers. These nanofibers were prepared via electrospinning and a subsequent selenization process and exhibited superior Na-ion storage properties compared to those of the bare densely structured NiSe$_2$ nanofibers. The synergetic effect of the porous structure of the composite nanofibers and the highly electrically conductive rGO-C matrix improved the electrochemical properties of the NiSe$_2$-rGO-C composite nanofibers for Na-ion storage applications. More importantly, the process developed in this study is
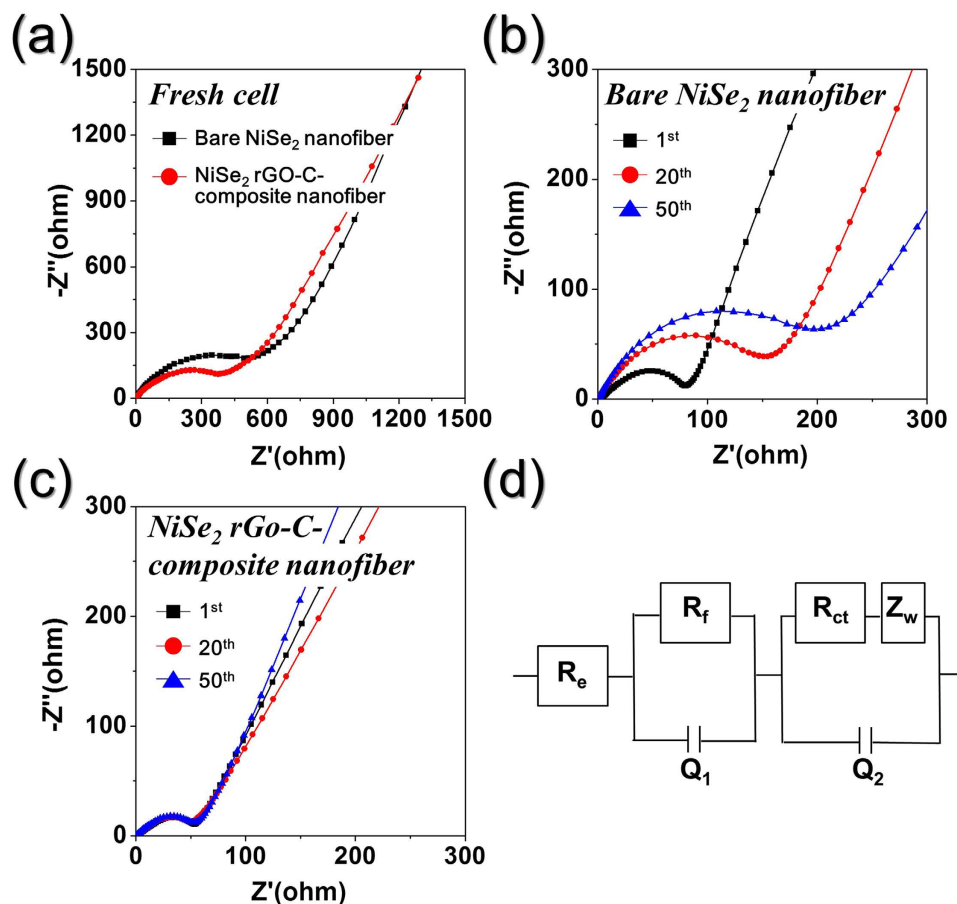
Figure 5. Nyquist impedance plots of the NiSe₂-rGO-C composite nanofibers and bare NiSe₂ nanofibers. (**a**) Nyquist impedance plots of the nanofibers before cycling, (**b**) Nyquist impedance plots of bare NiSe$_2$ nanofibers after cycling, (**c**) Nyquist impedance plots of NiSe$_2$-rGO-C composite nanofibers after cycling, and (**d**) equivalent circuit model used for AC impedance fitting.

applicable to both carbonaceous and non-carbonaceous metal selenide materials that can be used in various applications, including rechargeable secondary batteries.

Materials and Methods

Sample preparation. NiSe$_2$-reduced graphene oxide (rGO)-C composite nanofibers were prepared in a three-step process. During this process, nickel (II) acetate tetrahydrate-polyacrylonitrile-polystyrene with graphene oxide (GO) [Ni(OCOCH$_3$)$_2$·4H$_2$O-PAN-PS-GO] composite nanofibers were prepared as precursor fibers via electrospinning. GO was synthesized from graphite flakes using a modified Hummers method, as described in our previous report[36]. The precursor solution for the electrospinning process was prepared through vigorous overnight stirring of 1.5 g of Ni(OCOCH$_3$)$_2$·4H$_2$O (Aldrich, 99%), 1 g of PAN (polyacrylonitrile, Aldrich, M$_w$: 150,000), 4 g of PS (polystyrene, Aldrich, M$_w$: ~192,000), and 0.2 g of GO into a solution of 50 mL of N,N-dimethylformamide (DMF, Aldrich, 99%). The prepared solution was loaded at a flow rate of 2 mL h^{-1} into a plastic syringe equipped with a 25-gauge stainless steel nozzle, ejected, and subsequently electrospun onto a drum collector covered with Al foil. During the electrospinning process, the drum rotated at 100 rpm and a distance of 20 cm was maintained between the tip and the collector; a voltage of 25 kV was applied between the collector and the syringe tip. The first step in the post-treatment process was performed at 450 °C for 3 h under an Ar atmosphere, and yielded NiO$_x$-Ni nanosphere-decorated rGO-C composite nanofibers. In the second step of the process, these composite nanofibers were subjected to selenization at 300 °C for 10 h in H$_2$Se gas, which was formed from commercial Se metal powders and H$_2$ gas. For the selenization process, the composite nanofibers and Se metal powders were loaded into a covered alumina boat and placed in a quartz tube reactor; selenization resulted in the formation of NiSe$_2$ nanosphere-decorated rGO-C composite nanofibers. Bare NiSe$_2$ nanofibers were also synthesized for the sake of comparison. The nanofibers were prepared by electrospinning Ni(OCOCH$_3$)$_2$·4H$_2$O-PAN composite nanofibers, without PS and GO, under conditions identical to the aforementioned conditions. Bare NiSe$_2$ nanofibers were obtained by post-treating the resulting Ni(OCOCH$_3$)$_2$·4H$_2$O-PAN composite nanofibers at 450 °C for 3 h under an air atmosphere and then selenizing at 300 °C for 10 h in H$_2$Se gas.

Characterization. The microstructure of the nanofibers was examined via field emission scanning electron microscopy (SEM; Hitachi, S-4800) and field emission transmission electron microscopy (TEM; JEOL,
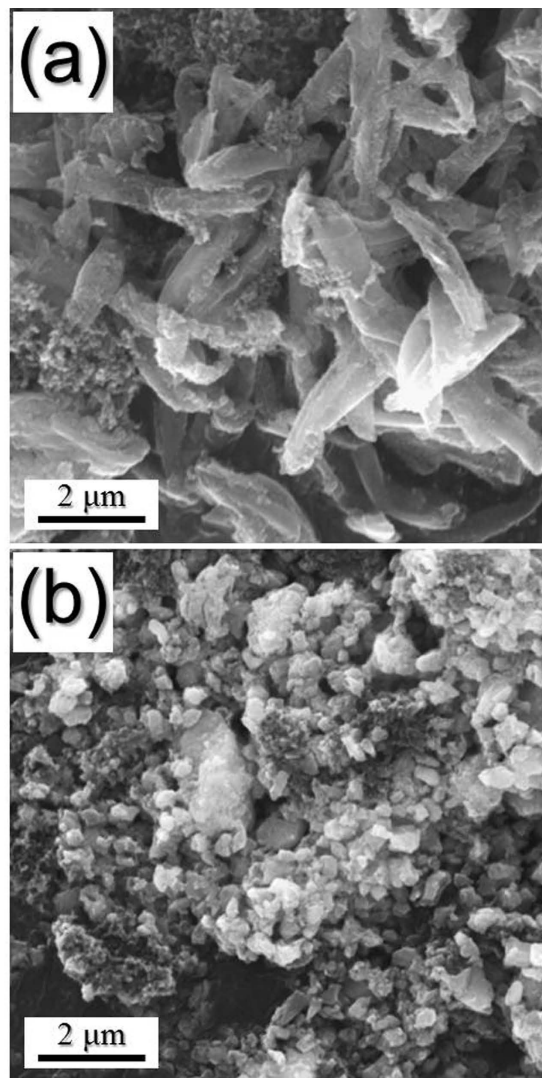
Figure 6. Morphologies of the (**a**) $NiSe_2$-rGO-C composite nanofibers and (**b**) bare $NiSe_2$ nanofibers with dense structure obtained after 100 cycles at a constant current density of $200\,mA\,g^{-1}$.

JEM-2100F). In addition, X-ray diffraction (XRD; X'Pert PRO MPD) using Cu K_α radiation ($\lambda = 1.5418\,Å$), performed at the Korea Basic Science Institute (Daegu), was used to evaluate the corresponding crystal structures. The composition of the specimens was determined via X-ray photoelectron spectroscopy (XPS; Thermo Scientific K-Alpha) performed with a focused monochromatic Al K_α beam operating at 12 kV and 20 mA. Moreover, the surface area of the nanofibers was determined by using the Brunauer–Emmett–Teller (BET) method, with N_2 as the adsorbate gas. The structure of the C in the specimens was characterized via Raman spectroscopy (Jobin Yvon LabRam HR800, excitation source: 632.8-nm He-Ne laser) performed at room temperature. Furthermore, thermogravimetric analysis (TGA) was performed using a Pyris 1 TGA (Perkin Elmer) at temperatures ranging from 25–650 °C at a heating rate of 10 °C min^{-1} under a static air atmosphere.

Electrochemical measurements. The electrochemical properties of the fabricated $NiSe_2$ nanofibers were determined by constructing a 2032-type coin cell. The anode was prepared by mixing the active material, carbon black, and sodium carboxymethyl cellulose (CMC) in a weight ratio of 7:2:1. Na metal and microporous polypropylene film were used as the counter electrode and the separator, respectively. Moreover, the electrolyte used consisted of 1 M $NaClO_4$ (Aldrich) dissolved in a mixture of ethylene carbonate/dimethyl carbonate (EC/DMC; 1:1 v/v), to which 5 wt% fluoroethylene carbonate (FEC) was added. The discharge/charge characteristics of the samples were investigated by cycling the cells at various current densities for potentials ranging from 0.001–3 V. The corresponding cyclic voltammograms (CV) were measured at a scan rate of 0.07 mV s^{-1}. The dimensions of the negative electrode were 1.5 cm × 1.5 cm and the mass loading was approximately 1.2 mg cm^{-2}. In addition, the electrochemical impedance over a frequency range of 0.01 Hz–100 kHz was measured via electrochemical impedance spectroscopy (EIS).

References

1. Li, L. *et al.* A flexible quasi-solid-state asymmetric electrochemical capacitor based on hierarchical porous V_2O_5 nanosheets on carbon nanofibers. *Adv. Energy Mater.* **5,** 1500753 (2015).
2. Xu, W. *et al.* Lithium metal anodes for rechargeable batteries. *Energy Environ. Sci.* **7,** 513–537 (2014).
3. You, Y., Wu, X. L., Yin, Y. X. & Guo, Y. G. High-quality Prussian blue crystals as superior cathode materials for room-temperature sodium-ion batteries. *Energy Environ. Sci.* **7,** 1643–1647 (2014).
4. Xu, Y. *et al.* Confined sulfur in microporous carbon renders superior cycling stability in Li/S batteries. *Adv. Funct. Mater.* **25,** 4312–4320 (2015).
5. Wei, T., Gong, Y., Zhao, X. & Huang, K. An all-ceramic solid-state rechargeable Na^+ battery operated at intermediate temperatures. *Adv. Funct. Mater.* **24,** 5380–5384 (2014).
6. Su, D., Dou, S. & Wang, G. Bismuth: A new anode for the Na-ion battery. *Nano Energy* **12,** 88–95 (2015).
7. Su, D., Ahn, H. J. & Wang, G. β-MnO_2 nanorods with exposed tunnel structures as high-performance cathode materials for sodium-ion batteries. *NPG Asia Mater.* **5,** e70 (2013).
8. Wang, L. *et al.* Porous CuO nanowires as the anode of rechargeable Na-ion batteries. *Nano Res.* **7,** 199–208 (2014).
9. Zhou, X. & Guo, Y. G. Highly disordered carbon as a superior anode material for room-temperature sodium-ion batteries. *ChemElectroChem* **1,** 83–86 (2014).
10. Xie, Q. *et al.* ZnO/Ni/C composite hollow microspheres as anode materials for lithium ion batteries. *J. Alloys Compd.* **619,** 235–239 (2015).
11. Xu, X. *et al. In situ* investigation of Li and Na ion transport with single nanowire electrochemical devices. *Nano Lett.* **15,** 3879–3884 (2015).
12. Islam, M. S. & Fisher, C. A. Lithium and sodium battery cathode materials: computational insights into voltage, diffusion and nanostructural properties. *Chem. Soc. Rev.* **43,** 185–204 (2014).
13. Anderson, B. D. & Tracy, J. B. Nanoparticle conversion chemistry: Kirkendall effect, galvanic exchange, and anion exchange. *Nanoscale* **6,** 12195–12216 (2014).
14. Li, S. *et al.* Effect of carbon matrix dimensions on the electrochemical properties of $Na_3V_2(PO_4)_3$ nanograins for high-performance symmetric sodium-ion batteries. *Adv. Mater.* **26,** 3545–3553 (2014).
15. Dahbi, M., Yabuuchi, N., Kubota, K., Tokiwa, K. & Komaba, S. Negative electrodes for Na-ion batteries. *Phys. Chem. Chem. Phys.* **16,** 15007–15028 (2014).
16. Saha, P. *et al.* Electrochemical performance of chemically and solid state-derived chevrel phase Mo_6T_8 (T = S, Se) positive electrodes for sodium-ion batteries. *J. Phys. Chem. C* **119,** 5771–5782 (2015).
17. Zhang, K., Hu, Z., Liu, X., Tao, Z. & Chen, J. $FeSe_2$ microspheres as a high-performance anode material for Na-ion batteries. *Adv. Mater.* **3,** 3305–3309 (2015).
18. Denis, Y. W. *et al.* High-capacity antimony sulphide nanoparticle-decorated graphene composite as anode for sodium-ion batteries. *Nat. Commun.* **4,** 2922 (2013).
19. Kim, Y. *et al.* SnSe alloy as a promising anode material for Na-ion batteries. *Chem. Commun.* **51,** 50–53 (2015).
20. Zhou, T. *et al.* Enhanced sodium-ion battery performance by structural phase transition from two-dimensional hexagonal-SnS_2 to orthorhombic-SnS. *ACS Nano* **8,** 8323–8333 (2014).
21. Zhang, J., Wang, Q., Wang, L., Li, X. A. & Huang, W. Layer-controllable WS_2-reduced graphene oxide hybrid nanosheets with high electrocatalytic activity for hydrogen evolution. *Nanoscale* **7,** 10391–10397 (2015).
22. Hu, Z. *et al.* Pyrite FeS_2 for high-rate and long-life rechargeable sodium batteries. *Energy Environ. Sci.* **8,** 1309–1316 (2015).
23. Ryu, H. S. *et al.* Degradation mechanism of room temperature Na/Ni_3S_2 cells using Ni_3S_2 electrodes prepared by mechanical alloying. *J. Power Sources* **244,** 764–770 (2013).
24. Zhang, J., Wang, L., Liu, X., Li, X. A. & Huang, W. High-performance CdS–ZnS core–shell nanorod array photoelectrode for photoelectrochemical hydrogen generation. *J. Mater. Chem. A* **3,** 535–541 (2015).
25. Bang, G. S. *et al.* Effective liquid-phase exfoliation and sodium ion battery application of MoS_2 nanosheets. *ACS Appl. Mater. Interfaces* **6,** 7084–7089 (2014).
26. Choi, S. H., Ko, Y. N., Lee, J. K. & Kang, Y. C. 3D MoS_2–graphene microspheres consisting of multiple nanospheres with superior sodium ion storage properties. *Adv. Funct. Mater.* **25,** 1780–1788 (2015).
27. Ko, Y. N., Choi, S. H., Park, S. B. & Kang, Y. C. Hierarchical $MoSe_2$ yolk–shell microspheres with superior Na-ion storage properties. *Nanoscale* **6,** 10511–10515 (2014).
28. Kim, J. S. *et al.* The discharge properties of Na/Ni_3S_2 cell at ambient temperature. *J. Power Sources* **178,** 852–856 (2008).
29. Xu, Y., Zhu, Y., Han, F., Luo, C. & Wang, C. 3D Si/C fiber paper electrodes fabricated using a combined electrospray/electrospinning technique for Li-ion batteries. *Adv. Energy Mater.* **5,** 400753 (2015).
30. Cho, J. S., Hong, Y. J. & Kang, Y. C. Design and synthesis of bubble-nanorod-structured Fe_2O_3–carbon nanofibers as advanced anode material for Li-ion batteries. *ACS Nano* **9,** 4026–4035 (2015).
31. Cho, J. S., Hong, Y. J. & Kang, Y. C. Electrochemical properties of fiber-in-tube-and filled-structured TiO_2 nanofiber anode materials for lithium-ion batteries. *Chem.-Eur. J.* **21,** 11082–11087 (2015).
32. Niu, C. *et al.* General synthesis of complex nanotubes by gradient electrospinning and controlled pyrolysis. *Nat. Commun.* **6,** 7402 (2015).
33. Xiong, X. *et al.* Flexible membranes of MoS_2/C nanofibers by electrospinning as binder-free anodes for high-performance sodium-ion batteries, *Sci. Rep.* **5,** 9254 (2015).
34. Yu, S., Jung, J. W. & Kim, I. D. Single layers of WS_2 nanoplates embedded in nitrogen-doped carbon nanofibers as anode materials for lithium-ion batteries. *Nanoscale* **7,** 11945–11950 (2015).
35. Ryu, W. H., Jung, J. W., Park, K., Kim, S. J. & Kim, I. D. Vine-like MoS_2 anode materials self-assembled from 1-D nanofibers for high capacity sodium rechargeable batteries. *Nanoscale* **6,** 10975–10981 (2014).
36. Xie, Q. *et al.* Hierarchical ZnO–Ag–C composite porous microspheres with superior electrochemical properties as anode materials for lithium ion batteries. *ACS Appl. Mater. Interfaces* **6,** 19895–19904 (2014).
37. Xie, Q. *et al.* Electrostatic assembly of sandwich-like Ag-C@ZnO-C@Ag-C hybrid hollow microspheres with excellent high-rate lithium storage properties. *ACS Nano* **10,** 1283–1291 (2016).
38. Park, G. D., Cho, J. S. & Kang, Y. C. Novel cobalt oxide-nanobubble-decorated reduced graphene oxide sphere with superior electrochemical properties prepared by nanoscale Kirkendall diffusion process. *Nano Energy* **17,** 17–26 (2015).
39. Yang, J. *et al.* Shape control and characterization of transition metal diselenides MSe_2 (M = Ni, Co, Fe) prepared by a solvothermal-reduction process. *Chem. Mater.* **13,** 848–853 (2001).
40. Lee, K. E. *et al.* Liquid crystal size selection of large-size graphene oxide for size-dependent N-doping and oxygen reduction catalysis. *ACS Nano* **8,** 9073–9080 (2014).
41. Park, G. D., Cho, J. S. & Kang, Y. C. Multiphase and double-layer $NiFe_2O_4$@ NiO-hollow-nanosphere-decorated reduced graphene oxide composite powders prepared by spray pyrolysis applying nanoscale Kirkendall diffusion. *ACS Appl. Mater. Interfaces* **7,** 16842–16849 (2015).
42. Cho, J. S., Hong, Y. J., Lee, J. H. & Kang, Y. C. Design and synthesis of micron-sized spherical aggregates composed of hollow Fe_2O_3 nanospheres for use in lithium-ion batteries. *Nanoscale* **7,** 8361–8367 (2015).

43. Guo, B. *et al.* Soft-templated mesoporous carbon-carbon nanotube composites for high performance lithium-ion batteries. *Adv. Mater.* **23,** 4661–4666 (2011).
44. Sun, Y., Hu, X., Luo, W., Xia, F. & Huang, Y. Reconstruction of conformal nanoscale MnO on graphene as a high-capacity and long-life anode material for lithium ion batteries. *Adv. Fuct. Mater.* **23,** 2436–2444 (2013).

Acknowledgements

Author Contributions

J.S.C. and Y.C.K. devised the concept, designed the experiment, and wrote the manuscript. J.S.C. and S.Y.L. performed the experiments and analyzed the data. Y.C.K. supervised the project. J.S.C. and Y.C.K. discussed the results and contributed in this manuscript.

Additional Information

Supplementary information accompanies this paper at http://www.nature.com/srep

Competing financial interests: The authors declare no competing financial interests.

How to cite this article: Cho, J. S. *et al.* First Introduction of NiSe₂ to Anode Material for Sodium-Ion Batteries: A Hybrid of Graphene-Wrapped NiSe₂/C Porous Nanofiber. *Sci. Rep.* **6,** 23338; doi: 10.1038/srep23338 (2016).